

Probing the Turbulent Ambipolar Diffusion Scale in Molecular Clouds with Spectroscopy

T. Hezareh^{1*}, T. Csengeri¹, M. Houde^{2,3}, F. Herpin⁴ and S. Bontemps⁵

¹*Max-Planck-Institut für Radioastronomie, Auf dem Hügel 69, 53121 Bonn, Germany*

²*Department of Physics and Astronomy, The University of Western Ontario, London, Ontario, Canada, N6A 3K7*

³*Division of Physics, Mathematics and Astronomy, California Institute of Technology, Pasadena, CA 91125, U.S.A.*

⁴*Université de Bordeaux, LAB, UMR 5804, F-33270, Floirac, France*

⁵*CNRS, LAB, UMR 5804, F-33270, Floirac, France*

ABSTRACT

We estimate the turbulent ambipolar diffusion length scale and magnetic field strength in the massive dense cores CygX-N03 and CygX-N53, located in the Cygnus-X star-forming region. The method we use requires comparing the velocity dispersions in the spectral line profiles of the coexistent ion and neutral pair H^{13}CN and H^{13}CO^+ ($J = 1 \rightarrow 0$) at different length scales. We fit Kolmogorov-type power laws to the lower envelopes of the velocity dispersion spectra of the two species. This allows us to calculate the turbulent ambipolar diffusion scale, which in turn determines the plane-of-the-sky magnetic field strength. We find turbulent ambipolar diffusion length scales of 3.8 ± 0.1 mpc and 21.2 ± 0.4 mpc, and magnetic field strengths of 0.33 mG and 0.76 mG for CygX-N03 and CygX-N53, respectively. These magnetic field values have uncertainties of a factor of a few. Despite a lower signal-to-noise ratio of the data in CygX-N53 than in CygX-N03, and the caveat that its stronger field might stem in part from projection effects, the difference in field strengths suggests different fragmentation efficiencies of the two cores. Even though the quality of our data, obtained with the IRAM Plateau de Bure Interferometer (PdBI), is somewhat inferior to previous single-dish data, we demonstrate that this method is suited also for observations at high spatial resolution.

Key words: ISM: clouds – ISM: magnetic fields – Submillimeter – Physical Data and Processes: turbulence – Line: profiles

1 INTRODUCTION

Our Galaxy contains about $1 - 3 \times 10^9 M_{\odot}$ of molecular gas (Bronfman et al. 1988), mostly in the form of giant molecular clouds that can be as massive as $10^{5-6} M_{\odot}$, and have Jeans mass of several 10s to 100 M_{\odot} . Therefore, cloud complexes should be highly gravitationally unstable, and if collapsing on free-fall time scales would result in a star formation rate of $M_{\star} \geq 200 M_{\odot} \text{ yr}^{-1}$ (Evans 1999). However, the observed star formation rate of $\sim 3 - 5 M_{\odot} \text{ yr}^{-1}$ (McKee 1989) in our Galaxy shows that the gravitational collapse time of these clouds must significantly exceed the free-fall time. Among the possible physical mechanisms of support against gravitational collapse in molecular clouds, interstellar magnetic fields and turbulence have been the most debated ones. The interplay between these mechanisms has

led to studying the combination of the two as one physical phenomenon (e.g., Goldreich & Sridhar 1995; Ostriker et al. 2001; Basu et al. 2009; Tilley & Balsara 2010; Li & Houde 2008; Houde et al. 2009; Hezareh et al. 2010; Houde et al. 2011; Li et al. 2012).

The study of magnetized turbulence in molecular clouds through the comparison of the line-widths of spectral line profiles of molecular ion and neutral species assumed to be coexistent (mainly the HCN/HCO^+ and $\text{H}^{13}\text{CN}/\text{H}^{13}\text{CO}^+$ pairs) started with the work of Houde et al. (2000a; 2000b). The conditions satisfying this assumption mainly include high correlation of the intensity maps of the two species, no sign of depletion of either of the tracers, and also the one to one correspondence of peak velocities of the spectral line profiles across the maps. Houde et al. (2000a; 2000b) introduced a model for turbulence in a weakly ionized gas in the presence of a magnetic field and discussed how in small enough scales where motions of the local turbulent

* E-mail: thezareh@mpifr-bonn.mpg.de (TH)

flow could be assumed linear, the ions would get trapped into gyromagnetic motion about the magnetic field rather than following the general neutral flow. It was shown that emission lines from an ion species will exhibit narrower profiles compared to that of a coexistent neutral species in regions with a magnetic field of a few tens of μG that is on average not aligned with the local flows. Houde et al. (2000a; 2000b) supported their model by detecting this ion line narrowing effect in the ($J = 3 \rightarrow 2$) and ($J = 4 \rightarrow 3$) transition lines of the HCN/HCO⁺ and H¹³CN/H¹³CO⁺ pairs of molecular species in several well-known molecular clouds.

In a more recent study, Li & Houde (2008) initiated a new observational technique based on recent simulations by Ostriker et al. (2001) and the work of Houde et al. (2000a; 2000b) to better investigate the effect of magnetic fields on the relative widths of ion and neutral spectral line profiles. They used the observational data for HCN and HCO⁺ ($J = 4 \rightarrow 3$) emission maps in M17 (Houde et al. 2002; Houde 2004), and plotted the velocity dispersions in the line profiles of the aforementioned species across the maps as a function of different beam sizes that translated into different spatial scales (hereafter referred to as velocity dispersion spectrum). At every spatial scale, a constant difference between the lower envelope of the velocity dispersion spectrum of the ion relative to that of the neutral was noted (see Figure 2 of Li & Houde (2008), and also Figures 4 and 5 of this work), which was interpreted as the ion and neutral flows dissipating their turbulent energy at different spatial scales. Assuming that the turbulent energy dissipation process is associated with ambipolar diffusion and that the ion velocity dispersion spectrum drops drastically at ambipolar diffusion scales, they used a Kolmogorov-type power law fit to their data to calculate the turbulent ambipolar diffusion length scale L_{AD} and the neutral velocity dispersion V_{AD} of a turbulent eddy at the corresponding length scale. More precisely, these parameters are obtained from the following equations (Li & Houde 2008)

$$\begin{aligned} L_{AD}^n &= -a/[b(1 - 0.37n)] \\ V_{AD}^2(L_{AD}) &= a + bL_{AD}. \end{aligned} \quad (1)$$

Here the parameters n (the spectral index), a (where $a < 0$), and b are the fitting parameters in the power law equations for the velocity dispersion spectra of the ions ($\sigma_i^2(L)$) and neutrals ($\sigma_n^2(L)$) given by

$$\begin{aligned} \sigma_i^2(L) &= bL^n + a \\ \sigma_n^2(L) &= bL^n. \end{aligned} \quad (2)$$

In order to calculate the strength of the magnetic field using the obtained parameters, Li & Houde (2008) started with the magnetic Reynolds number

$$R_m = 4\pi n_i \mu \nu_i LV / B^2, \quad (3)$$

which is effectively the ratio of the importance of magnetic flux freezing to magnetic diffusivity at a given length scale. Here L and V are characteristic length and velocity scales for a given Reynolds number, respectively, n_i is the ion density, ν_i and μ are the collision rate of an ion with the neutrals and the mean reduced mass characterizing such collisions, respectively. We assume the gas to be well coupled to the field lines at large scales and that the ion-neutral decoupling

occurs at turbulent energy dissipation length scales. Numerical simulations by Li et al. (2008) have shown a range of Reynolds numbers ($0.12 < R_m < 12$) for which ambipolar diffusion effects become important in the clump morphology, the effect becoming more important as the Reynolds number decreases. Following Li & Houde (2008), we assume that the decoupling scale $L = L_{AD}$ corresponds to $R_m = 1$, where the magnetic diffusion overcomes the flux freezing, hence the onset of the decoupling of ions from neutrals. This choice of the R_m value can introduce an uncertainty of a factor of a few in our calculations. We proceed to derive an equation for the field strength in the plane of the sky as a function of interstellar physical parameters by substituting $R_m = 1$, $n_i = n_n \chi_e$, where χ_e is the ionization fraction and n_n the neutral volume density, $\nu_i = 1.5 \times 10^{-9} n_n \text{ s}^{-1}$ (Nakano 1984), and mean ion and neutral atomic mass numbers $A_i = 29$ and $A_n = 2.3$, respectively. Using typical parameters for giant molecular clouds (GMCs), we obtain

$$B_{\text{pos}} = \left(\frac{L_{AD}}{0.5 \text{ mpc}} \right)^{1/2} \left(\frac{V_{AD}}{1 \text{ kms}^{-1}} \right)^{1/2} \left(\frac{n_n}{10^6 \text{ cm}^{-3}} \right) \times \left(\frac{\chi_e}{10^{-7}} \right)^{1/2} \text{ mG}. \quad (4)$$

One concern regarding this technique was the fact that the spectral lines of HCN and HCO⁺ usually appear to be optically thick and saturated. To investigate whether the constant difference between the velocity dispersion spectra of the ion and the neutral was consistent with similar observations using different species, Hezareh et al. (2010) tested the turbulent energy dissipation model of Li & Houde (2008) by mapping the optically thin isotopologues H¹³CN and H¹³CO⁺ ($J = 4 \rightarrow 3$) in DR21(OH). Their analysis showed that the difference between the velocity dispersion of the H¹³CN and H¹³CO⁺ spectral lines at different length scales displayed a similar result as originally obtained by Li & Houde (2008) with the optically thick HCN and HCO⁺ lines. They concluded that the narrowing of ion lines relative to neutrals, which was first discussed by Houde et al. (2000a) is a real physical effect and confirmed the results in the works of Li & Houde (2008).

In this paper, we examine the interferometry data from the ($J = 1 \rightarrow 0$) transition of H¹³CN and H¹³CO⁺ in the Cygnus X star forming region previously obtained and reduced by Csengeri et al. (2011) in order to test this technique at higher spatial resolutions, i.e., at smaller physical scales. We present our observations in §2. The data analysis is explained and results are presented in §3, a discussion in §4 and we end with a summary in §5.

2 OBSERVATIONS

Cygnus-X is a massive molecular cloud complex located at a distance of 1.4 kpc (Rygl et al. 2012). The first continuum observations of this region were performed by Motte et al. (2007), who used an infrared extinction map produced from 2MASS data and selected the high column density ($A_V \geq 15$ mag) clouds of Cygnus-X and mapped them in 1.2 mm continuum emission using the IRAM 30-m telescope. Bontemps et al. (2010) followed up these studies by performing high-angular resolution continuum observations

with the IRAM Plateau de Bure Interferometer (PdBI) at 1.3 and 3.5 mm towards the six most massive and youngest (IR-quiet) dense cores (MDCs) in the complex. These MDCs are fragmented and are shown to host early phase massive protostars. Their fragmentation properties have been discussed extensively by Bontemps et al. (2010), where they propose that a mechanism of support against self gravity (such as magnetic fields, turbulence, or radiative feedback) additional to thermal pressure is required to explain the formation of massive protostars larger than the local Jeans masses. The selected dense cores have sizes of about 0.13 pc, average density of $1.9 \times 10^5 \text{ cm}^{-3}$, and masses of 60–200 M_{\odot} . Detection of SiO emission in these sources confirms the presence of outflows, which suggests them to be actively forming stars (Motte et al. 2007). However, the lack of strong mid-IR and free-free emission indicates that they must be in an early stage of their evolution. Csengeri et al. (2011) mapped these selected cores in H^{13}CN and H^{13}CO^+ emission with the PdBI to study the kinematic properties of the dense gas surrounding the massive protostars.

For this work we required intensity maps of dense cores hosting protostellar objects in which H^{13}CO^+ was not affected by CO depletion or other chemical effects, causing significant differences in spatial distribution of the two tracers. The emission maps should also be sufficiently spatially extended while maintaining a high enough signal-to-noise ratio to provide enough number of pixels for a better statistical spectral line-width analysis explained in §1. Among the sources observed by Csengeri et al. (2011), two had sufficiently extended and correlated ion and neutral emission maps and were therefore suitable for our analysis. These were CygX-N03 and CygX-N53, located at ($20^{\text{h}}35^{\text{m}}34.1^{\text{s}}$, $42^{\circ}20'05.0''$) and ($20^{\text{h}}39^{\text{m}}03.1^{\text{s}}$, $42^{\circ}25'50.0''$) (J2000), respectively. CygX-N03 is located close to DR17, an HII region, which is excited by two OB clusters (Le Duigou & Knödseder 2002) while the latter is located in the DR21 filament, the most massive and densest region of Cygnus-X and a well-known region of massive star formation (Schneider et al. 2010). Table 1 summarizes some of the physical parameters in the aforementioned sources obtained from single dish observations (Motte et al. 2007).

The observations were carried out with the PdBI at 3 mm. The sources were mapped in H^{13}CN ($J = 1 \rightarrow 0$) and H^{13}CO^+ ($J = 1 \rightarrow 0$) at 86.75 GHz and 86.34 GHz, respectively, with a velocity resolution of 0.134 km s^{-1} . The observations were done in track-sharing mode with two targets per track. More details on the antennae setup and preliminary data reduction can be found in Bontemps et al. (2010) and Csengeri et al. (2011).

3 ANALYSIS & RESULTS

The data reduction and analysis of the interferometric data was performed with the GILDAS¹ software. Csengeri et al. (2011) reduced the interferometric H^{13}CO^+ dataset both with and without adding short-spacing information, which was obtained with the IRAM 30-m telescope. Since no zero-spacing information was available for the H^{13}CN dataset,

the H^{13}CO^+ maps were used without this short spacing correction for the purpose of a consistent dataset. The maps were corrected for primary beam attenuation and a natural weighting was used for the image reconstruction. The selected sources were observed in different tracks on different days, therefore the synthesized beam sizes are slightly different. The size of the synthesized beams in CygX-N03 were $3.7'' \times 3.0''$ with a position angle of 63° for both species and $4.2'' \times 3.3''$ with a position angle of 69° in CygX-N53. The baselines ranged from 24 m to 229 m and the uv coverage was the same for H^{13}CO^+ and H^{13}CN in each source. The fraction of flux filtered out in the interferometry data for H^{13}CO^+ was examined by comparing the integrated intensities in the single dish and PdBI spectra at the same offsets. The PdBI spectra contain 78% and 72% of the integrated intensity of single dish spectra in CygX-N03 and CygX-N53, respectively. We also consider the implications of combining single-dish and interferometry data in Section 4.3.

3.1 Correlation of the Intensity Maps

Figure 1 shows the intensity maps of H^{13}CN ($J = 1 \rightarrow 0$) and H^{13}CO^+ ($J = 1 \rightarrow 0$) in CygX-N03, and the intensity maps of the same molecular pair in CygX-N53 are displayed in Figure 2. Although the HCO^+ and HCN pair and their isotopologues are observed to have the highest large scale spatial correlation among other pairs of ions and neutrals (Lo et al. 2009), some differences between their distribution still exist, particularly at higher resolutions such as the observations we present here. The H^{13}CN intensity maps include the integrated flux from all three hyperfine lines, where the intensities of the three components follow the ratios 1 : 5 : 3. However, in CygX-N53 the intensities of the H^{13}CN hyperfine lines vary slightly from this ratio due to optical depth effects. This may be the cause for the difference in the location of peak intensities in the H^{13}CN and H^{13}CO^+ maps in this source. The spectral line data for CygX-N53 have a lower signal-to-noise ratio than the spectra in CygX-N03, and required a careful analysis for investigating the coexistence criteria of the observed ion and neutral species.

In order to check the consistency of our maps, we calculated the linear correlation coefficients for the pairs of maps across a $10'' \times 10''$ area around the peak positions in CygX-N03 and CygX-N53. We obtain correlation coefficients of 0.84 and 0.82 for the maps in CygX-N03 and CygX-N53, respectively, to confirm that the maps correlate well within the regions in our analysis. As a more extensive test, the peak velocities of the H^{13}CO^+ lines were compared to those of the central hyperfine component of H^{13}CN across the maps for both sources. The correlation plots for the peak velocities of the two tracers in each source are presented in Figure 3. The plotted peak velocities correspond to spectral lines for which we obtained 3σ velocity dispersion values, i.e., the data points we use for our analysis. The uncertainty values for the peak velocity measurements are included and a linear least squares fit to the data points yields $y = (1.23 \pm 0.03)x + (0.18 \pm 0.06)$ for CygX-N03 and $y = (0.96 \pm 0.05)x - (0.14 \pm 0.14)$ for CygX-N53. The scatter plot for CygX-N53 is affected by the lower data quality in this source. The fitting uncertainties do not take into account the velocity resolution of 0.14 km s^{-1} for our spec-

¹ <http://iram.fr/IRAMFR/GILDAS/>

tral lines, and the peak velocities are measured from the expected systemic velocity for the sources for a more meaningful estimate of the intercept. Given the aforementioned uncertainties, these results are in general consistent with our assumption of H^{13}CO^+ and H^{13}CN being coexistent in the two sources.

3.2 Velocity Dispersion Calculations

The intensity maps are oversampled with beam spacings of $0.62''$, which is useful for our analysis. Since the aim of this work is to characterize turbulence with spectral line profiles, in order to find the location of minimum turbulence level we must find the position of the spectral line with the narrowest line-width that corresponds to both species. Following the technique introduced by Ostriker et al. (2001) and further tested by Falceta-Gonçalves et al. (2010) within the context of the Li & Houde (2008) method, we scan across the source with the finest resolution available by calculating the line-widths of spectral line profiles in every pixel of the map.

In each map, the velocity dispersions of the spectral line profiles are calculated within an area of $10'' \times 10''$ around the central core, as specified by the black frames in Figures 1 and 2. The size of these enclosed areas were determined by the extent of the H^{13}CN spectra with high enough signal-to-noise ratio that enabled comparison with H^{13}CO^+ spectra at corresponding positions. To mimic spectra at different beam sizes, we applied the technique in Li & Houde (2008) and Hezareh et al. (2010) in using a boxcar-like function to average the spectra of neighboring pixels in the regions restricted by the black frames across the intensity maps. More precisely, we started with a 110-pixel map for each tracer and each source at the actual beam resolution ($3.3''$ for CygX-N03 and $3.8''$ for CygX-N53). We then averaged every 4 neighboring pixels of the original map to reduce the map resolution to 30 pixels at $3.9''$ for CygX-N03 and $4.5''$ for CygX-N53. We further averaged 9 and 16 neighboring pixels to produce 16- and 9-pixel maps with resolutions of $4.6''$ and $5.2''$, respectively, for CygX-N03 and similar maps with resolutions of $5.1''$ and $5.7''$, respectively, for CygX-N53.

We ran a GILDAS script on all the H^{13}CO^+ and the central component of H^{13}CN hyperfine spectral lines to fit three Gaussian components to each line. The spectral lines that needed fewer than three components returned fitting results with zero-amplitude profiles (with respect to the baseline) for the extra components. This way, we obtained between 1 and 3 Gaussian profiles for each spectral line. We calculated the integrated residual flux in the spectral lines using the aforementioned Gaussian fits, and got an average value of 4 mK, which compared to the rms noise level of ~ 100 mK is insignificant, thus confirming the reliability of our fits. The corresponding H^{13}CN and H^{13}CO^+ lines do not necessarily have the same number of Gaussian fits and were treated independently, and the overall velocity dispersion, σ , for a given line was calculated as the weighted average of the velocity dispersions of the Gaussian components about the mean, the weights being the area under each Gaussian profile.

The plots of the square of the velocity dispersions (σ^2) as a function of length scale (simulated beam sizes) are shown in the top panels of Figures 4 and 5, with the H^{13}CN data plotted in black and H^{13}CO^+ in red. The measurement

uncertainties in these plots are only displayed in the lower panels for a clearer representation of the data points. The scatter of data points at each length scale above the lower envelopes is a reflection of the range of line-widths measured at that scale.

According to equation (4), the observed ambipolar diffusion scale length varies with B_{pos} (thus a further dependency on the inclination angle of the field), the density, and the ionization rate. Since the value of σ^2 of the ion results from the integration of the turbulent spectrum from the ambipolar diffusion scale to that of the telescope beam, spatial variations in any of these parameters will strongly affect the width of the ion line, while leaving the neutral line unaffected (i.e., the neutral line-width is not dependent on the ambipolar diffusion scale). Despite these facts, we note that the spectral lines of both species with the minimum σ^2 values are found to be located in the same vicinity within the resolution of the original and also all smoothed maps, as shown in dashed circles in Figures 1 and 2, adding further support to the assumption of coexistence of H^{13}CN and H^{13}CO^+ in our sources. Figure 6 displays the ion and neutral spectral lines at this location from the highest resolution maps for each source, where the H^{13}CO^+ spectra are plotted in red and H^{13}CN in black. The latter is scaled to the temperature of H^{13}CO^+ for a better comparison of their corresponding line widths. The three resolved hyperfine lines of H^{13}CN are clearly displayed, and the H^{13}CO^+ line-width is compared to that of the central component of H^{13}CN at all offsets.

3.3 Turbulent Ambipolar Diffusion and Magnetic Field Calculations

For a closer inspection, the Kolmogorov-type power law fits to the lower envelopes of the ion and neutral velocity dispersion spectra are plotted together with the values of σ^2 and their corresponding uncertainties at every length scale in the bottom panels of Figures 4 and 5. The ambipolar diffusion model of Li & Houde (2008) predicts the same power-law fit for both species in the inertial range. Therefore, we first fitted the difference between the square of the velocity dispersion data of H^{13}CN and H^{13}CO^+ to a constant function to obtain parameter a , and then fitted the sum of the two data sets to a power law of the form $2bL^n + a$ to obtain b and n . The results for the fitting parameters in Equation (2) for both sources are shown in Table 2. A comparison between these parameters for the two sources shows that the difference between the lower envelopes of the ion and neutral σ^2 spectra (parameter a) in CygX-N53 is noticeably larger than that in CygX-N03, while the spectral indices (parameter n) are similar. This leads to a larger ambipolar diffusion scale $L_{AD} = 2.92'' = 21.20 \pm 0.35$ mpc in CygX-N53, compared to $L_{AD} = 0.53'' = 3.84 \pm 0.06$ mpc in CygX-N03. These values are consistent with the calculations of Houde et al. (2011) and Li & Houde (2008) in other star forming regions. Assuming similar ionization fractions of 10^{-7} (McCall et al. 1999) and adopting the hydrogen number densities from Motte et al. (2007) (see Table 1), we calculate B_{pos} of 0.33 mG and 0.76 mG for CygX-N03 and CygX-N53, respectively. This value can be inaccurate up to an order of magnitude due to the uncertainties in n_n and χ_e , and the fact that Equation (4) is derived with the

assumption of determining the turbulent ambipolar diffusion length scale where the effective magnetic Reynolds number is $\simeq 1$ (Li & Houde 2008), which is an approximation.

It is worth noting that CygX-N53 is located $\simeq 3'$ north of DR21(OH), the source studied by Hezareh et al. (2010). The analysis in DR21(OH) was performed with the source distance taken to be 3 kpc (Genzel & Downes 1977), while for this work we took the new distance of 1.5 kpc obtained with trigonometric parallax measurements of Rygl et al. (2012). After applying the distance correction to the calculations for DR21(OH), the turbulent ambipolar diffusion scale becomes $\simeq 8.5$ mpc, and we obtain a magnetic field of 0.67 mG as opposed to the previous value of 1.7 mG obtained earlier by Hezareh et al. (2010). Although the new field strength for DR21(OH) is more consistent with the value for CygX-N53 given their location in a common filament (DR21), it also indicates another source of uncertainty in the ambipolar diffusion length and magnetic field measurements, i.e., measurements of source distances.

4 DISCUSSION

4.1 The Essence of This Technique

This is the first high resolution study on the determination of the turbulent ambipolar diffusion and magnetic field strength from the velocity dispersion spectra of a pair of co-existent interstellar ion and neutral molecules. An idealized situation for this study would consist of pointing the smallest available telescope beam at the appropriate location in a cloud and measuring the velocity dispersion through the observed spectral line profile, and then perform several subsequent observations at the same location but with a series of increasingly larger beams. It would be best if the subsequent beam sizes differed by a small amount, i.e., smaller than a beam size, as this set of measurements would then allow one to finely build up the dispersion relation and determine the appropriate Kolmogorov-type scaling law. In this work, this resolution is set by the sampling rate on our maps, which is about $0.6''$ or approximately one-fifth of the telescope beam size. We effectively come as close as possible to achieve this once we find the location of minimum turbulence level with the finest grids. But since these locations are away from the centre of the maps and we are still limited by the signal-to-noise ratio of the spectra outside the aforementioned frames, we cannot expand our analysis with a higher precision around these locations.

The fact that we do not possess a large range of scales, say over several beam sizes, is admittedly a limitation in our analysis as it restricts the domain over which we can characterize turbulence with a Kolmogorov-type law. It is, however, well-suited to determine the turbulent ambipolar diffusion decoupling scale in these cores. This is especially relevant since the highest resolution observations performed in this study were realized with a telescope beam size closest to the expected range for the turbulent ambipolar diffusion length scale, when compared to previous studies.

Across the intensity maps, pixels with higher intensity are likely to be locations with longer lines of sight through the cloud, where turbulent sub-structures (or eddies) of larger sizes can exist (Falceta-Gonçalves et al. 2010), which

will in turn lead to broader spectral lines (i.e., larger velocity dispersions). In other words, the different lines of sight intercept several turbulent substructures of different velocities, causing an increase in the observed velocity dispersions. Therefore, the unique minimum values that we calculate for σ^2 at every length scale may be attributed to the line of sight that intercepts the fewest number of such turbulent sub-structures (Falceta-Gonçalves et al. 2010). It is important to realize that the measured line-widths change significantly over even a fraction of the beam extent. For example, at the smallest beam size of $3.3''$, velocity dispersion values vary from 0.75 km s^{-1} to 2.71 km s^{-1} across ten consecutive pixels (similar size of $3.3''$) for CygX-N03 in H^{13}CN , therefore the overlapping beams in our oversampled map do not cause redundancy in our calculations.

We point out the recent discovery of a hyperfine structure in H^{13}CO^+ ($J = 1 \rightarrow 0$) in the form of a doublet splitting of 0.133 km s^{-1} by Schmid-Burgk et al. (2004). This unresolved splitting contributes to the overall line-width we calculate for every H^{13}CO^+ line. However, despite this unresolved splitting, the line profiles of H^{13}CO^+ were found to be narrower than those of H^{13}CN across the intensity maps providing further support to the idea of the ion line narrowing effect due to the presence of magnetic fields.

4.2 Significance of the Magnetic Field in the Two Sources

It is possible to compare the magnetic energy with the gravitational and kinetic energies when the full strength of the magnetic field is measured in a source. In this study we only measure the plane-of-the-sky component of the field, so we apply the less precise approach of estimating the full field strength using statistical expectation values of $|\mathbf{B}| = (4/\pi)B_{\text{pos}}$ and $|\mathbf{B}|^2 = (3/2)B_{\text{pos}}^2$ for any random orientation of the B-field (Crutcher et al. 1999). Of course, these are only probable values and do not necessarily apply to an individual core but since our calculations are accurate within a factor of a few, and given the uncertainties in the derived size and mass of these sources, we can nevertheless perform an approximate energy comparison in the observed sources. Table 3 summarizes the estimates for the ratio of mass to the magnetic flux ratio $M/\Phi_B = 1.0 \times 10^{-20} N(\text{H}_2) / |\mathbf{B}| \text{ cm}^2 \mu\text{G}$, in units of the critical value $(M/\Phi_B)_{\text{crit}} \approx 0.12/\sqrt{G}$ (Crutcher et al. 1999; Mouschovias & Spitzer 1976), which is a measure of the relative importance of gravitational to magnetic energy. The ratio of the magnetic to kinetic energies is also calculated for each source as (Stahler & Palla 2005)

$$\frac{\mathcal{M}}{\mathcal{T}} \simeq \frac{|\mathbf{B}|^2 R^3}{3M\sigma^2}, \quad (5)$$

where the cores are assumed to be spherical with M the mass, R the size, and σ the observed one dimensional velocity dispersion (taken from Csengeri et al. (2011)). We calculated M and $N(\text{H}_2)$ using the number densities from Motte et al. (2007) and taking $R \simeq 10''$ as inferred from our Figures 1 and 2. The results in Table 3 imply that both sources are magnetically supercritical ($M/\Phi_B > 1$), i.e. gravitationally unstable, and there is an equipartition of the kinetic and magnetic energies in CygX-N03 while

the magnetic energy dominates the kinetic energy in CygX-N53. Given the different fragmentation properties of the two cores (Csengeri et al. 2011), it is possible that magnetic fields play a more important role in the fragmentation of CygX-N53 compared to CygX-N03. Our magnetic field measurements alone are consistent with the findings of Csengeri et al. (2011) and Bontemps et al. (2010) in that CygX-N53 exhibits a higher core fragmentation efficiency than CygX-N03 as we measure a stronger field in the former source.

Although our sources are known to have similar masses (Motte et al. 2007), CygX-N03 exhibits a smaller turbulent ambipolar diffusion length scale and a weaker B_{pos} strength compared to CygX-N53. As a further study, the line-of-sight component of the magnetic field in these sources can be obtained through Zeeman observations to clarify whether it is the difference in the orientation of the field or in the total strength of the magnetic field that sets the distinction in the observed cores. Currently, Zeeman measurements on CN ($J = 1 \rightarrow 0$) in the aforementioned sources are underway, and the forthcoming results will be published in a future paper.

4.3 Combining single-dish and interferometry data

The extended molecular emission is spatially filtered out in the interferometry observations, therefore the larger scale turbulence is missing from the line profiles. Since we are looking for the location of minimum turbulence, i.e., the spectra with the narrowest line-widths, this flux filtering in principle should not hurt our analysis. Moreover, referring to Figure 3 of Li & Houde (2008), it can be noted that the measured velocity dispersion at any scale is the integral of the power spectrum from the beam scale to the diffusion scale in the k space. It follows that if interferometry observations would only filter out the large scale components of the turbulent spectrum, then one would naively expect that line widths confined to the unfiltered portion of the spectrum would be unaffected whether or not single-dish observations were included.

But the large-scale flux filtering also implies a reduction of the depth into the cloud that is probed by the observations. Interferometric observations to which single-dish data are added should therefore be expected to yield larger line widths for a given spatial scale (i.e., beam size), which would manifest themselves, for example, through an increased value for parameter b in Equation (1). In other words, single-dish observations will probe more turbulent sub-structures deeper in the gas probed by the telescope beam than corresponding interferometric measurements (Falceta-Gonçalves et al. 2010); this also implies that the two types of measurements will not probe exactly the same volume of gas (and medium).

On the one hand, if the nature of the turbulence is unchanged with depth in the gas, then we would expect that it preserves its logarithmic index n when single-dish data are added. Since this implies that the shape of the turbulent spectrum is preserved then the a and b parameters would be scaled up by the same factor, as they both result from integrations of the turbulent power spectrum (Li & Houde 2008). We would then find that the ambipolar diffusion scale

L_{AD} would also remain unchanged (see Equation (1)), while the estimate for the magnetic field strength in Equation (4) would increase with the square-root of the factor by which a and b are scaled up (through V_{AD} in Equation (1)).

On the other hand, the picture is not so clear when the nature of turbulence changes with depth in the cloud. Although we expect both a and b to be larger, it cannot generally be assumed that they will increase with the same factor. It is, however, safe to surmise that both the logarithmic slope n and the ambipolar diffusion scale L_{AD} will vary and observationally reveal values intermediate to those that would be measured with interferometric and single-dish data independently.

We tested the above arguments using H^{13}CO^+ maps of combined single-dish and interferometric data of Csengeri et al. (2011) and we found that for both sources the line widths increase significantly, as expected. In the case of CygX-N03 we found that $b = 0.19 \text{ km}^2 \text{ s}^{-2} \text{ arcsec}^{-n}$ (compared to $0.09 \text{ km}^2 \text{ s}^{-2} \text{ arcsec}^{-n}$ for interferometry data alone) and $n = 0.54$ (basically unchanged from $n = 0.52$). These results are therefore in line with the discussion above when the nature of turbulence is unchanged with depth in the cloud. It also implies from Equation (4) that the magnetic field strength resulting from the inclusion of single-dish data would increase by a factor of $\sqrt{0.19/0.09} = 1.45$; this is not an unreasonable change in view of the general expectation that magnetic field strengths increase with density.

Interestingly for CygX-N53, it is b that is almost unchanged with the inclusion of single-dish data ($0.25 \text{ km}^2 \text{ s}^{-2} \text{ arcsec}^{-n}$ instead of $0.24 \text{ km}^2 \text{ s}^{-2} \text{ arcsec}^{-n}$), while the logarithmic slope n varies significantly from the previous value of 0.52 to 0.30. It is therefore apparent that for this source turbulence exhibits different characteristics with depth in the cloud. Unfortunately, the lack of single-dish data for H^{13}CN does not allow us to determine a corresponding value for a and we therefore cannot estimate the ambipolar diffusion scale or the magnetic field strength in this case.

4.4 Consistency with Related Works

It is interesting to note that current anisotropic MHD turbulence models (Goldreich & Sridhar 1995; Cho et al. 2002; Cho & Lazarian 2003; Kowal & Lazarian 2010) all predict longer correlation length scales along the magnetic field than across it. Additionally, Heyer et al. (2008) investigated velocity anisotropy induced by MHD turbulence in the Taurus molecular cloud using computational simulations and molecular line observations. Indeed, they measured a velocity anisotropy aligned within $\sim 10^\circ$ of the mean magnetic field orientation obtained from optical polarization measurements. It is expected that (ambipolar) diffusion length scales would follow a similar pattern as they are also related to the width of correlation functions. Assuming the physical conditions in the two sources to be the same, our measurements of a shorter dissipation scale in CygX-N03 might then be another indication that its magnetic field tends to align itself closer to the line of sight than that of CygX-N53 (for a given field strength).

Recent MHD simulations using the heavy-ion approximation (Li et al. 2006) performed at different Reynolds numbers by Li et al. (2012) find that their numerical simulations for the ion turbulent spectrum do not fall off as

steeply as assumed by Li & Houde (2008). However, even if that were the case, we expect that our determination of the turbulent ambipolar dissipation scale using the model of Li & Houde (2008) will still be a characteristic length scale representative of the spectral dissipation range. As a result, future interferometry observations at higher resolutions will be crucial in probing sub-arc second scales, which will in turn enable us to investigate the behavior of the ion and neutral velocity dispersion spectra at the decoupling length scales.

The coexistence of HCO^+ and HCN (not including their isotopologues) was recently investigated for different spatial scales and core central densities using chemical and dynamical models of evolving prestellar molecular cloud cores including non-equilibrium chemistry and magnetic fields (Tassis et al. 2012). It was shown that the abundances of the two species were indeed well correlated on large scales (1 pc) but the correlation was weaker for sub-parsec scales. Additionally, Tassis et al. (2012) predicted new ion-neutral pairs that are good candidates for such observations because they reveal similar evolutionary trends and are approximately co-spatial in their models. These candidate pairs include HCO^+/NO , HCO^+/CO , and NO^+/NO . Further observations are needed to test these chemical models and will especially help investigate the nitrogen-driven chemistry in the ISM.

4.5 Limitations

In this section we note the limitations of this study in certain star forming regions, in particular dense cores in which the selected ion and neutral species do not show a sign of coexistence. This can occur in sources with significant depletion of CO and its isotopologues, as a result of which species such as HCO^+ and H^{13}CO^+ will trace the envelopes while HCN and H^{13}CN stay close to the inner (colder and denser) part of the cores.

Moreover, star forming regions are usually associated with molecular outflows that are revealed with far-infrared observations. Outflows leave their signature as high velocity wings on spectral line profiles. In the context of ambipolar diffusion, the effect of outflows on the relative line widths of the observed ion and neutral spectra has been discussed in some of the early papers on the subject (e.g., Houde et al. 2001, 2002, 2004). While HCN often traces outflows preferentially over HCO^+ (e.g., Walker-Smith et al. (2013)), there also exists examples where the line profiles of both species appear to be equally affected (see for example the case of NGC 2071 in Houde et al. (2001)). Although we cannot be completely certain of this, given the spectra presented in our Figure 6 we believe it is reasonable to assume that outflows do not play an important role in explaining the differences in line widths. Perhaps the best indication for this assertion is our result that the turbulent power spectra for both molecular species can be modelled with the same values for b and n . Such results would be unlikely if that were not the case.

We also note that recent observations of $^{12}\text{CO}(2 \rightarrow 1)$ with the PdBI in both CygX-N03 and CygX-N53 reveal bipolar molecular outflows (Duarte-Cabral et al. 2013), which were not seen earlier with H^{13}CN and H^{13}CO^+ ($J = 1 \rightarrow 0$). Since the outflow signature in our interferometry

dataset was inconspicuous, we did not apply any correction for its effect.

5 SUMMARY

We analyzed interferometric maps of H^{13}CN ($J = 1 \rightarrow 0$) and H^{13}CO^+ ($J = 1 \rightarrow 0$) in CygX-N03 and CygX-N53, two dense cores in the Cygnus-X star forming region, as a further test for the turbulent energy dissipation model of Li & Houde (2008). A constant difference between the ion and neutral velocity dispersion spectra is observed in both sources (Figures 4 and 5), and the turbulent ambipolar diffusion scale and plane-of-the-sky magnetic field strengths are calculated. Although the magnetic field strengths are uncertain up to an order of magnitude, we can still address the issue of additional support for these MDCs, previously raised by Bontemps et al. (2010). We conclude that magnetic fields and turbulent motions are equally important in the fragmentation of CygX-N03, while the higher core fragmentation efficiency in CygX-N53 previously measured by Bontemps et al. (2010) is consistent with a stronger magnetic field dominating the turbulent motions in this core.

ACKNOWLEDGEMENTS

The authors thank the referee for a careful reading and insightful comments. T.H. was funded by the Alexander von Humboldt foundation. T.Cs.'s contribution was funded by ERC Advanced Investigator Grant GLOSTAR (247078). M. H.'s research is funded through the NSERC Discovery Grant, Canada Research Chair, Canada Foundation for Innovation, and Western's Academic Development Fund programs.

REFERENCES

- Bontemps, S., Motte, F., Csengeri, T., & Schneider, N. 2010, *A&A*, 524, 18
- Bronfman, L., Cohen, R. S., Alvarez, H., May, J., & Thaddeus, P. 1988, *ApJ*, 324, 248
- Basu, S., Ciolek, G., E., Dapp, W. B., & Wurster, J. 2009, *NewA*, 14, 483
- Cho, J., Lazarian, A., & Vishniac, E. T. 2002, *ApJ*, 564, 291
- Cho, J., & Lazarian, A. 2003, *MNRAS*, 345, 325
- Crutcher, R. M., Troland, T. H., Lazareff, B., Paubert, G., & Kazés, I. 1999, *ApJ*, 514, 121
- Csengeri, T., Bontemps, S., Schneider, N., Motte, F., & Dib, S. 2011, *A&A*, 527, 135
- Duarte-Cabral, A., Bontemps, S., Motte, F., Hennemann, M., Schneider, N., & André, Ph. 2013, *A&A*, 558, 125
- Evans, N. J. II 1999, *ARA&A*, 37, 311
- Falseta-Gonçalves, D., Lazarian, A., & Houde, M. 2010, *ApJ*, 713, 1376
- Genzel, R., & Downes, D. 1977, *A&AS*, 30, 145
- Goldreich, P., & Sridhar, S. 1995, *ApJ*, 438, 763
- Heyer, M., Gong, H., Ostriker, E., & Brunt, C. 2008, *ApJ*, 680, 420
- Hezareh, T., Houde, M., McCoey, C., & Li, H. 2010, *ApJ*, 720, 603

- Houde, M., Bastien, P., Peng, R., Phillips, T. G., & Yoshida, H. 2000a, *ApJ*, 536, 857
- Houde, M., Peng, R., Phillips, T. G., Bastien, P., & Yoshida, H. 2000b, *ApJ*, 537, 245
- Houde, M., Phillips, T. G., Bastien, P., Peng, R., & Yoshida, H. 2001, *ApJ*, 547, 311
- Houde, M., Bastien, P., Dotson, J. L., et al. 2002, *ApJ*, 569, 803
- Houde, M. 2004, *ApJ*, 616, 111
- Houde, M., Dowell, C. D., Hildebrand, R. H., Dotson, J. L., Vaillancourt, J. E. et al. 2004, *ApJ*, 604, 717
- Houde, M., Vaillancourt, J. E., Hildebrand, R. H., Chitsaz-zadeh, S., & Kirby, L. 2009, *ApJ*, 706, 1504
- Houde, M., Rao, R., Vaillancourt, J. E., & Hildebrand, R. H. 2011, *ApJ*, 733, 109
- Kowal, G., & Lazarian, A. 2010, *ApJ*, 720, 742
- Le Duigou, J., & Knödlseider, J. 2002, *A&A*, 392, 869
- Li, P. S., McKee, C. F., & Klein, R. I. 2012, *ApJ*, 744, 73
- Li, P. S., McKee, C. F., Klein, R. I., & Fisher, R. T. 2008, *ApJ*, 684, 380
- Li, P. S., McKee, C. F., & Klein, R. I. 2006, *ApJ*, 653, 1280
- Li, H., & Houde, M. 2008, *ApJ*, 677, 1151
- Lo, N., Cunningham, M. R., Jones, P. A., et al. 2009, *MNRAS*, 395, 1021
- McCall, B. J., Geballe, T. R., Hinkle, K. H., & Oka, T. 1999, *ApJ*, 522, 338
- McKee, C. F. 1989, *ApJ*, 345, 782
- Motte, F., Bontemps, S., Schilke, P., et al. 2007, *A&A*, 476, 1243
- Mouschovias, T. Ch., & Spitzer, L., Jr. 1976, *ApJ*, 210, 326
- Nakano, T. 1984, *Fundam. Cosmic Phys.*, 9, 139
- Ostriker, E. C., Stone, J. M., & Gammie, C. F. 2001, *ApJ*, 546, 980
- Rygl, K. L. J., Brunthaler, A., Sanna, A., et al. 2012, *A&A*, 539, 79
- Schmid-Burgk, J., Muders, D., Müller, H. S. P., & Brupbacher-Gatehouse, B. 2004, *A&A*, 419, 949
- Schneider, N., Csengeri, T., Bontemps, S., et al. 2010, *A&A*, 520, 49
- Stahler, S. W. & Palla, F. 2005, *The Formation of Stars* (Weinheim, Germany: Wiley-VCH)
- Tassis, K., Hezareh, T., & Willacy, K. 2012, *ApJ*, 760, 57
- Tilley, D. A., & Balsara, D. S. 2010, *MNRAS*, 406, 1201
- Walker-Smith, S., Richer, J., Buckle, J., Salji, C., Hatchell, J., & Drabek, E. 2013, *Protostars and Planets VI*, Heidelberg, Poster 1B001

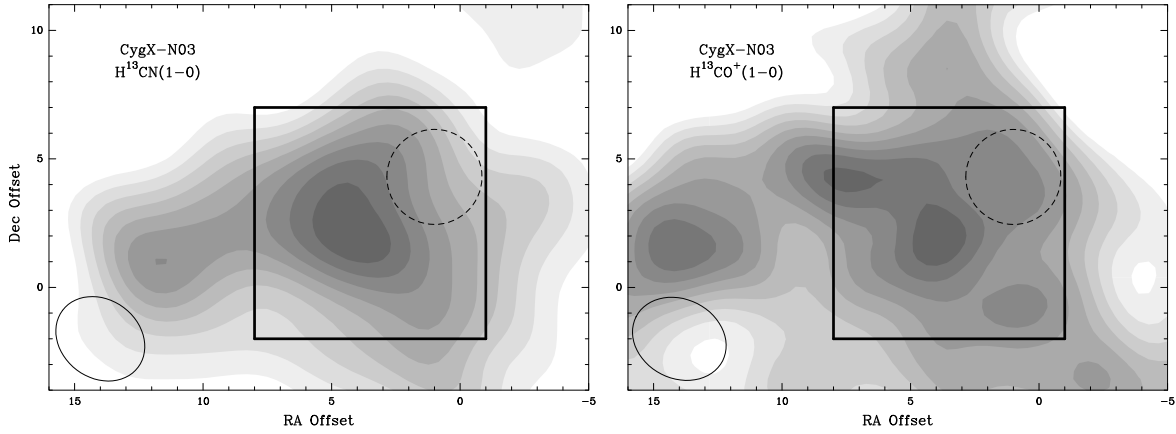


Figure 1. Comparison of the intensity maps of H^{13}CN and H^{13}CO^+ ($J = 1 \rightarrow 0$) integrated over a velocity range of 10 km s^{-1} to 30 km s^{-1} in CygX-N03. The contours span a range of 10% to 90% of the peak ($13.28 \text{ K km s}^{-1}$ for H^{13}CN and 6.05 K km s^{-1} for H^{13}CO^+) by increments of 10%. The beam footprint is shown by the ellipses in the bottom left corners of the maps. The rectangular frames mark the areas in the maps chosen for our analysis and the dashed circles display the location along the line of sight where the minimum values of the velocity dispersions are obtained observationally. The offsets are with respect to the reference positions stated in Table 1.

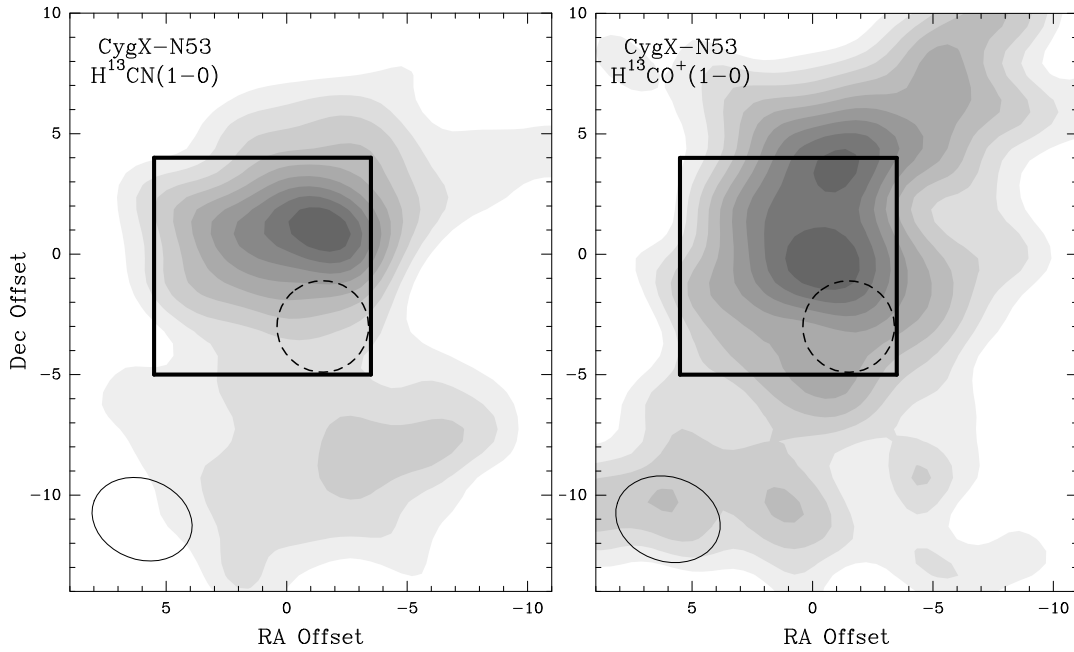


Figure 2. Comparison of the intensity maps of H^{13}CN and H^{13}CO^+ ($J = 1 \rightarrow 0$) integrated over a velocity range of -20 km s^{-1} to 20 km s^{-1} in CygX-N53. The contours span a range of 10% to 90% of the peak ($13.13 \text{ K km s}^{-1}$ for H^{13}CN and 5.37 K km s^{-1} for H^{13}CO^+) by increments of 10%. The beam footprint is shown by the ellipses in the bottom left corners of the maps. The rectangular frames mark the areas in the maps chosen for our analysis and the dashed circles display the location along the line of sight where the minimum values of the velocity dispersions are obtained observationally. The offsets are with respect to the reference positions stated in Table 1.

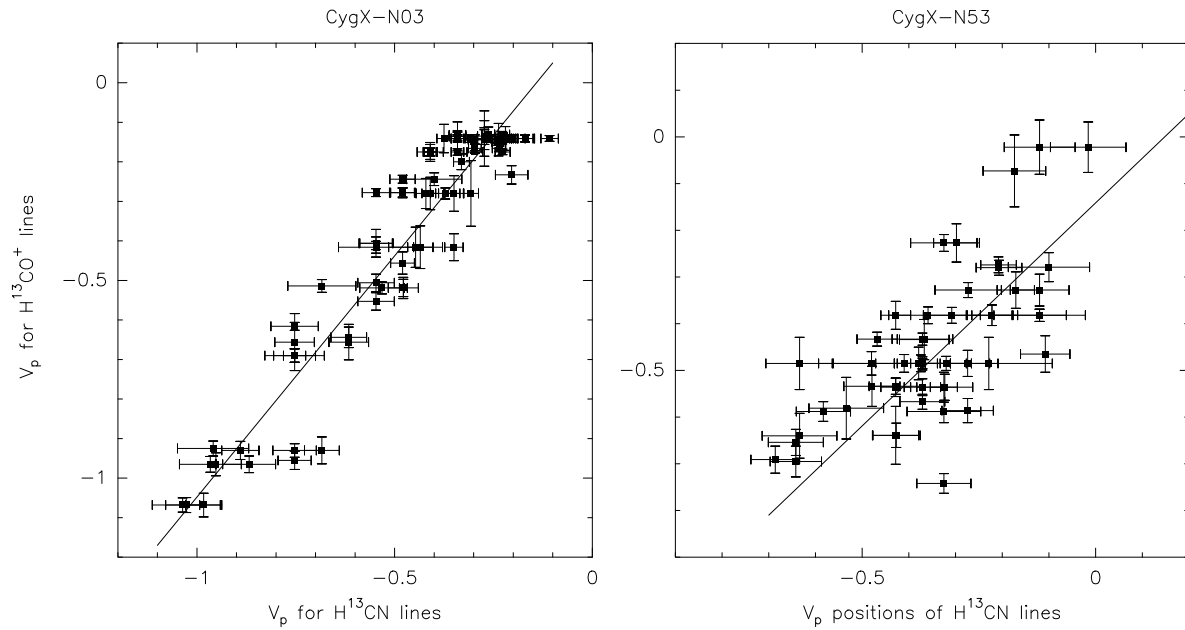


Figure 3. **Left:** Comparison of the peak velocities (V_p) of the H^{13}CO^+ and H^{13}CN spectral lines in CygX-N03. A linear least squares fit to the data yields $y = (1.23 \pm 0.03)x + (0.18 \pm 0.06)$. **Right:** Same plot for CygX-N53, where the regression line follows the equation $y = (0.96 \pm 0.05)x - (0.14 \pm 0.14)$. In both figures the plotted velocities correspond to data points whose velocity dispersions are 3σ values.

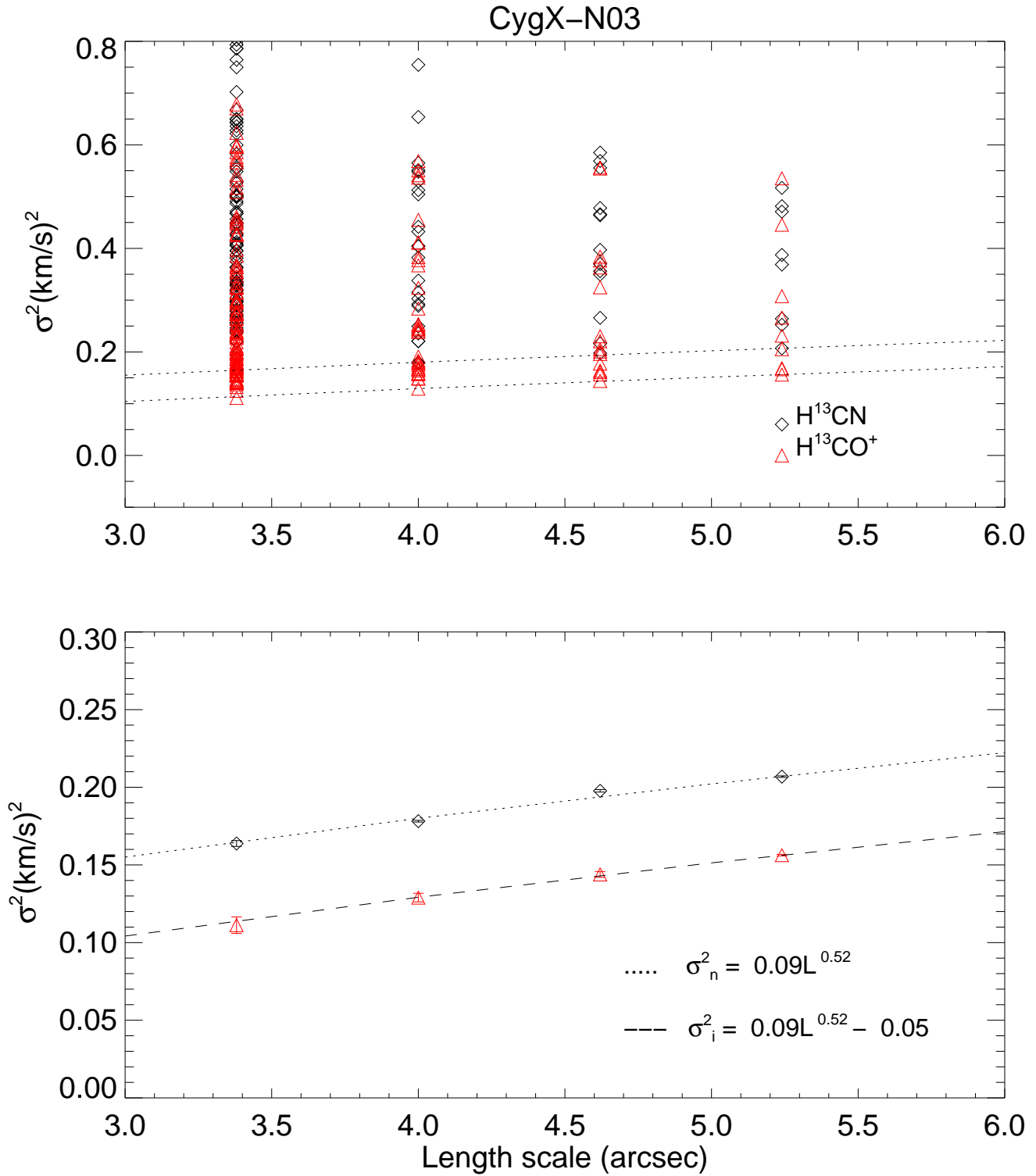


Figure 4. Top: Plot of σ^2 as a function of length scale in CygX-N03. The measurement uncertainties for the data points are not shown to avoid clutter in the graph. **Bottom:** The lower envelopes of the H^{13}CN and H^{13}CO^+ data fitted for Kolmogorov-type power laws.

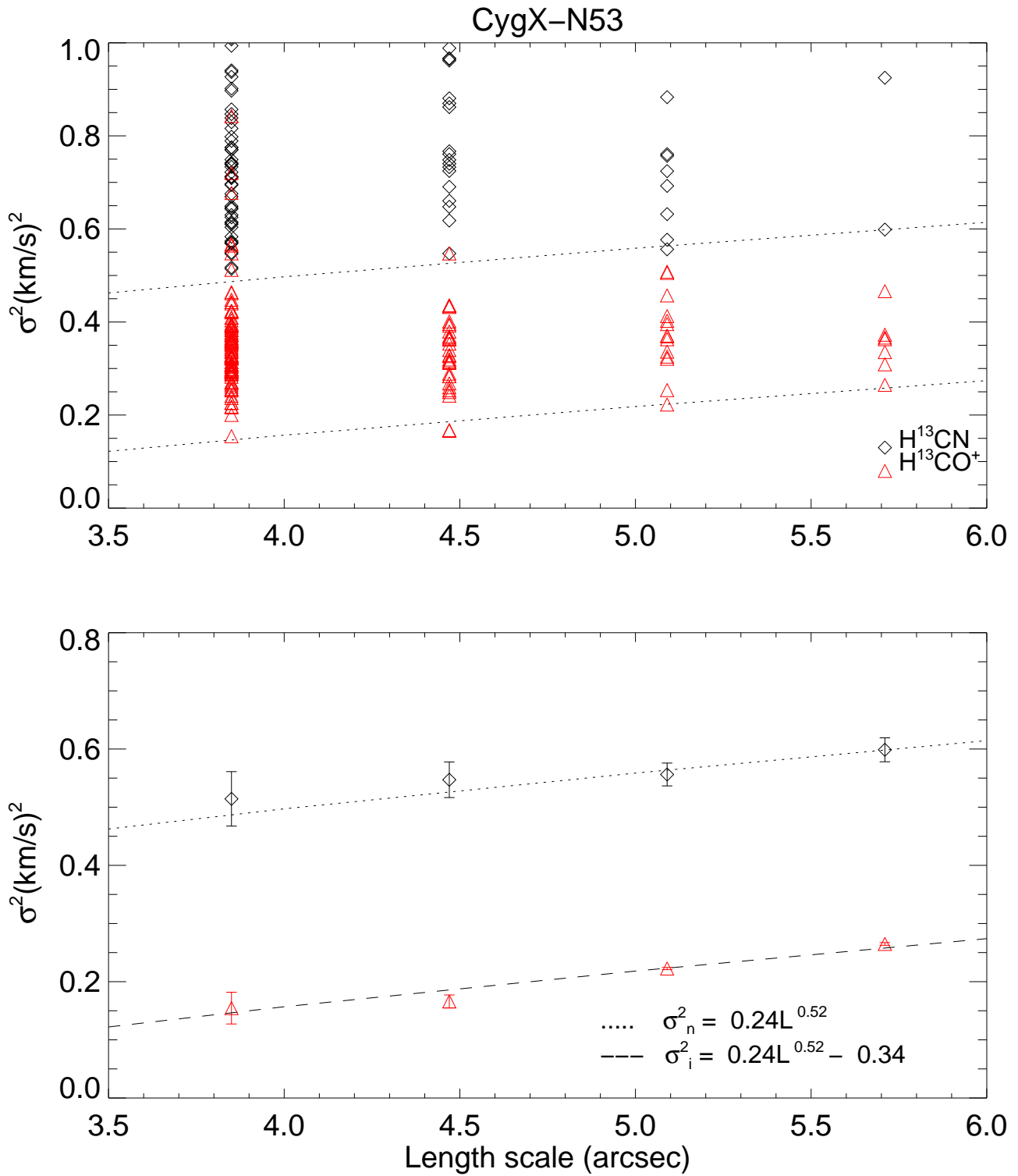


Figure 5. Same as Figure 4, but for Cyg-N53.

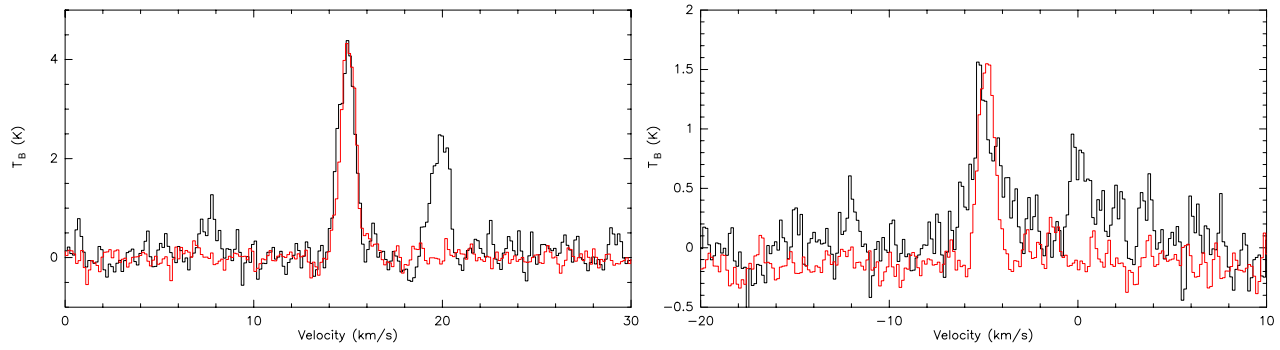


Figure 6. Comparison of the line widths of the $J = 1 \rightarrow 0$ transition of H^{13}CO^+ (red) and H^{13}CN (black) spectral lines corresponding to the minimum σ^2 values at the smallest beam size in CygX-N03 (left) and CygX-N53 (right). The H^{13}CN lines are scaled to the H^{13}CO^+ line temperatures for a clearer line width comparison. Of the three hyperfine lines of H^{13}CN , we compare the line-width of the central component with that of H^{13}CO^+ at all beam sizes.

Table 1. Physical parameters of the sources obtained from single dish continuum observations

Source ^a	RA J(2000)	Dec J(2000)	$M_{1.2\text{ mm}}$ M_{\odot}	Deconvolved FWHM size pc×pc	n_{H_2} cm^{-3}
CygX-N03	20:35:34.1	42:20:05.0	84	0.11×0.09	3.6×10^5
CygX-N53	20:39:03.1	42:25:50.0	85	0.14×0.09	2.2×10^5

^a Masses, sizes and number densities are obtained by Motte et al. (2007)

Table 2. Data reduction parameters for the observed sources

Source	a $\text{km}^2 \text{ s}^{-2}$	b $\text{km}^2 \text{ s}^{-2} \text{ arcsec}^{-n}$	n	V_{AD} km s^{-1}	L_{AD} mpc	B_{pos} μG
CygX-N03	-0.051 ± 0.001	0.088 ± 0.005	0.520 ± 0.036	0.11	3.84 ± 0.06	331.30
CygX-N53	-0.340 ± 0.009	0.241 ± 0.026	0.522 ± 0.064	0.28	21.20 ± 0.35	765.32

Table 3. Comparison of the magnetic energy to kinetic and gravitational energies

Source	M/Φ_B ($\text{cm}^2 \mu\text{G}$)	\mathcal{M}/\mathcal{T}
CygX-N03	3.8	0.9
CygX-N53	1.6	10.1